Journal of
Instrumentation

OPEN ACCESS

High-Z sensors at MHz repetition rate FELs: first AGIPD results

To cite this article: D. Magalhaes *et al* 2026 *JINST* **21** C01019

View the article online for updates and enhancements.

You may also like

- Theoretical analysis of optogenetic spiking with ChRmine, bReaChES and CsChrimson-expressing neurons for retinal prostheses
Himanshu Bansal, Neha Gupta and Sukhdev Roy
- AGIPD, a high dynamic range fast detector for the European XFEL
A. Allahgholi, J. Becker, L. Bianco et al.
- Performance tests of an AGIPD 0.4 assembly at the beamline P10 of PETRA III
J Becker, A Marras, A Klyuev et al.

This content was downloaded from IP address 131.169.131.155 on 23/01/2026 at 12:33

Jinst

PUBLISHED BY IOP PUBLISHING FOR SISSA MEDIALAB

RECEIVED: September 30, 2025
REVISED: December 4, 2025
ACCEPTED: December 16, 2025
PUBLISHED: January 19, 2026

26TH INTERNATIONAL WORKSHOP ON RADIATION IMAGING DETECTORS
BRATISLAVA, SLOVAKIA
6–10 JULY 2025

High-Z sensors at MHz repetition rate FELs: first AGIPD results

D. Magalhaes,[a,b,*] **H. Hirsemann**,[a,b] **A. Klujev**,[a,b] **Z. Konopkova**,[c] **S. Lange**,[a,b] **T. Laurus**,[a,b] **M. Niemann**,[a,b] **S. Palutke**,[c] **D. Pennicard**,[a,b] **M. Ramilli**,[c] **V. Rovensky**,[c] **C. Strohm**,[a] **J. Sztuk-Dambietz**,[c] **U. Trunk**,[a,b] **M. Veale**,[d] **M. Wilson**[d] **and H. Graafsma**[a,b,e]

[a] *Deutsches Elektronen-Synchrotron DESY, Notkestrasse 85, 22607 Hamburg, Germany*
[b] *Center for Free-Electron Laser Science (CFEL), c/o DESY, Bldg. 99, Luruper Chaussee 149, 22761 Hamburg, Germany*
[c] *European XFEL GmbH, Holzkoppel 4, 22869 Schenefeld, Germany*
[d] *Rutherford Appleton Laboratory, UKRI Science & Technology Facilities Council, Oxon, OX11 0QX, U.K.*
[e] *Mid Sweden University, 851 70 Sundsvall, Sweden*

E-mail: debora.magalhaes@desy.de

ABSTRACT: To address new applications in the 18–30 keV photon energy range at the European XFEL, where silicon sensors lose quantum efficiency, the AGIPD Collaboration has developed an AGIPD detector prototype with high-Z sensor materials. An electron-collecting version of the chip (ecAGIPD) was designed to leverage from the higher mobility and longer lifetime of electrons with respect to holes in the candidate materials: chromium-doped gallium arsenide (GaAs:Cr) and high-flux cadmium zinc telluride (CdZnTe). This work reports on the characterization of GaAs and high-flux CdZnTe ecAGIPD prototypes at the HED instrument at the European XFEL. Their time response, linearity and performance at 2.2 and 4.5 MHz frame rates were evaluated. Preliminary results demonstrate good linearity of both materials up to 1.6e+03 15 keV photons/mm^2/pulse, and a residual after-pulse signal corresponding to less than one photon on CdZnTe, up to an estimated flux of 1.2e+05 24 keV photons/mm^2/pulse.

KEYWORDS: Materials for solid-state detectors; Instrumentation for FEL; X-ray detectors; Hybrid detectors

*Corresponding author.

© 2026 The Author(s). Published by IOP Publishing Ltd on behalf of Sissa Medialab. Original content from this work may be used under the terms of the Creative Commons Attribution 4.0 licence. Any further distribution of this work must maintain attribution to the author(s) and the title of the work, journal citation and DOI.

https://doi.org/10.1088/1748-0221/21/01/C01019

2026 JINST 21 C01019

Contents

1 Introduction **1**

2 Materials and methods **3**

3 Results and discussion **4**
3.1 Intensity scans 5
3.2 Timing scans 5
3.3 After-signal measurements 7

4 Conclusion and further steps **9**

A Sensor material properties considered in this work **10**

1 Introduction

The first Adaptive Gain Integrating Pixel Detector (AGIPD) system [1] was installed and commissioned at the European XFEL (EuXFEL) in 2017, and has been successfully deployed at three experimental stations: Single Particles, Clusters, and Biomolecules & Serial Femtosecond Crystallography (SPB/SFX) [2], Materials Imaging and Dynamics (MID) [3], and High Energy Density Science (HED) [4] since then. Detector systems of different sizes have been delivered, and both the ASIC and the overall system have been upgraded over the years, with the latest version being 1.2. To date, all AGIPD systems have pixels of 200 µm and use hole-collecting ASICs bump-bonded to 500 µm-thick p-on-n silicon sensors.

The HED instrument is designed to probe matter under extreme conditions of pressure, temperature, and electromagnetic fields. Combined with hard X-ray free-electron laser radiation, it provides a unique experimental platform that supports multiple techniques, including diffraction, scattering, spectroscopy, and imaging [4]. The distinct pulse structure of the EuXFEL further enables time-resolved studies with MHz time resolution.

HED experiments also envisage operation in the hard X-ray energy range of 18–30 keV. In this regime, the quantum efficiency of standard silicon sensors drops significantly (figure 1). This reduction in absorption has two major consequences: (i) reduced photon statistics, and (ii) increased exposure of ASIC electronics behind the sensors to radiation, which shortens the detector lifespan and raises the need for spare modules. To address these limitations, sensors made from high-atomic-number (high-Z) materials are required.

While the use of high-Z sensors is commonplace in the synchrotron community, their use at FELs has to date been extremely limited. Initial measurements made at Linac Coherent Light Source (LCLS) using CdZnTe and GaAs:Cr sensors demonstrated encouraging performance [5], but these measurements were limited to pulse repetition rates of 120 Hz. How these sensor materials perform at the MHz repetition rates delivered by the EuXFEL is yet to be established, and is the focus of this work.

2026 JINST 21 C01019

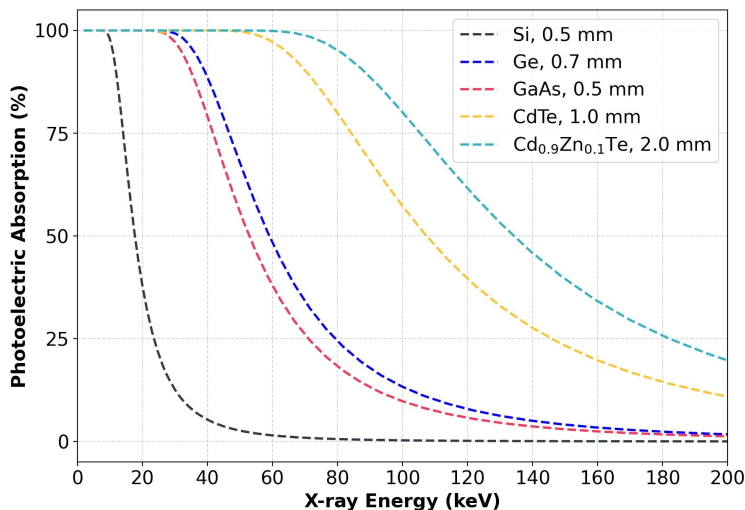

Figure 1. Photoelectric absorption of commonly used sensor materials as a function of the photon energy. Data from NIST [6].

2026 JINST 21 C01019

Several candidate sensor materials are used in the hybrid detector community, and a comparison of their photoelectric absorption at the usual thicknesses is shown in figure 1. Germanium was excluded due to its small band gap (0.67 eV), which requires substantial cooling to suppress intrinsic noise [7]. The remaining candidates — GaAs, CdTe, and $Cd_{0.9}Zn_{0.1}Te$ — are compound semiconductors, and their growth processes can introduce crystal defects. Such defects act as charge-carrier traps, reducing charge-collection efficiency or, in severe cases, distorting the bias electric field to the point of polarization.

The mobility of positive charge carriers (holes) is lower compared to that of negative charge carriers (electrons) in all such sensor materials (see appendix A), meaning that holes are more prone to be trapped by defects. Collecting electrons in sensors with high defect concentrations therefore becomes a more reliable option, and the AGIPD Collaboration chose to develop an electron-collecting version of the ASIC, namely *ecAGIPD*, for high-energy applications.

As a charge-integrating, gain-switching pixel detector, AGIPD is well suited for sensor characterization. It provides direct access to the deposited energy at the pixel level with sufficient resolution across a wide energy range. In addition, the MHz frame rate of the ASIC enables detailed sub-microsecond studies of charge transport in the sensor, while also being less sensitive to sensor leakage current due to the small integration time. While the current version of the ecAGIPD ASICs suffers from a design limitation in the gain-bits memory matrix, preventing reliable gain recovery in Adaptive Gain mode, they remain valuable for sensor material characterization studies, which were conducted mostly at fixed Gain mode.

In this work, GaAs and $Cd_{0.9}Zn_{0.1}Te$ (CZT) sensors were investigated. The first is widely adopted for high-energy synchrotron applications [8, 9], while high-flux CdZnTe, recently introduced by Redlen Technologies, has emerged as a promising option for high-flux applications such as 4th generation synchrotrons and FELs [5, 10, 11]. Attempts were made to include CdTe sensors for comparison, but they were discarded due to very high leakage current and will not be approached in this study.

2 Materials and methods

Single-chip GaAs and CZT sensors were bump-bonded to ecAGIPD ASICs by ADVAFAB OY and mounted on AGIPD front-end modules (FEMs). In addition, four high-flux CZT quad sensors (2 mm thick) from Redlen Technologies, compatible with 2×2 ecAGIPD chips, were either stud-bonded by Polymer Assembly Technology at 80 °C, or bump-bonded by ADVAFAB or STFC-UKRI at 150 to 160 °C. This diversity of bonding methods and temperatures allows a later evaluation of their impact on detector performance. All CZT sensors have platinum contacts on both sides.

The FEMs were first characterized in terms of leakage current, ASIC configuration and charge collection efficiency using an Amptek Mini-X2 X-ray source. Based on such tests, four FEMs were selected and integrated into a 500k AGIPD prototype housing [12] for dedicated beamtimes at the HED instrument. The final selection of FEMs is listed in table 1. Figure 2(a) shows the assembled prototype, with the 4 FEMs mounted on the left side of the detector head, including custom electronic boards designed in-house to filter and route the sensor bias voltage from an external power supply to the cathodes.

A stand-alone FEM composed of 500 µm thick hole-collecting Si sensors bump-bonded to 2×8 AGIPD 1.1 chips (commercialized by ©X-Spectrum as SPARTA) was used as a reference. Figure 2(b) shows the covered prototype, with a vertical tantalum stripe that partially covers the active area of the sensors, and the SPARTA module mounted below the detector stage. Pixels within the covered region were used as a frame-wise monitor of the baseline level.

Table 1. Composition of the FEMs selected for the characterization beamtimes.

FEM Sensor	Year	Thickness (µm)	Bonded by	Bias Voltage
GaAs:Cr, singles	2017	500	Advafab	-300 V
CZT, singles (CZT1)	2019	2000	Advafab	-800 V
hf-CZT, quad (CZT2)	2024	2000	Polymer Assembly T.	-1000 V
hf-CZT, quad (CZT3)	2024	2000	Advafab	-1000 V
p-on-n type Si	2022	500	IZM	+200 V

This study reports results from two dedicated beamtimes at the HED experimental station:

- November 2024, proposal 900478: 2.2 MHz repetition rate, photon energies of 18 keV and 24 keV. Data collected using Yttrium fluorescence (14.98 keV) and LaB_6 powder diffraction;
- February 2025, proposal 900516: 2.2 MHz repetition rate, photon energy of 8.07 keV, about 5× higher intensity. Data collected using scattering from a glassy carbon sample.

The first session served to verify the functionality of high-Z sensors in the target energy range, while the second probed their flux limits by operating at lower photon energies but higher fluxes.

The experimental campaign included: (i) flat-field measurements; (ii) intensity scans using the beamline attenuators; (iii) scans of the acquisition window in time with respect to the pulses (here referred-to as timing scans); and (iv) after-pulse measurements, to verify the remaining signal after irradiation for different scenarios. During operation, the detector was cooled by a chiller with liquid coolant set to 14 °C.

2026 JINST 21 C01019

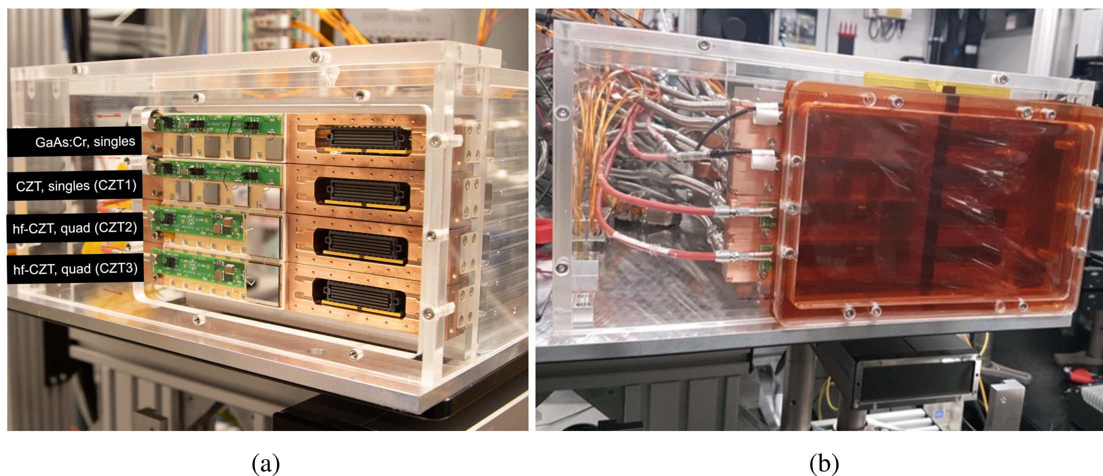

Figure 2. High-Z mini-half prototype installed at HED experimental hutch: (a) without the protection lid, showing the high-Z FEMs mounted on the left side of the detector head; (b) with the polyimide protection windows and a vertical tantalum stripe partially covering the sensors. The SPARTA module can be seen below the detector table.

3 Results and discussion

Images of Y fluorescence from a single YAG (Yttrium Aluminum Garnet) crystal (14.98 keV) and of LaB_6 powder diffraction at 24 keV, both taken with the source frequency set to 2.2 MHz, are shown in figure 3. The integration time for both acquisitions was 200 ns.

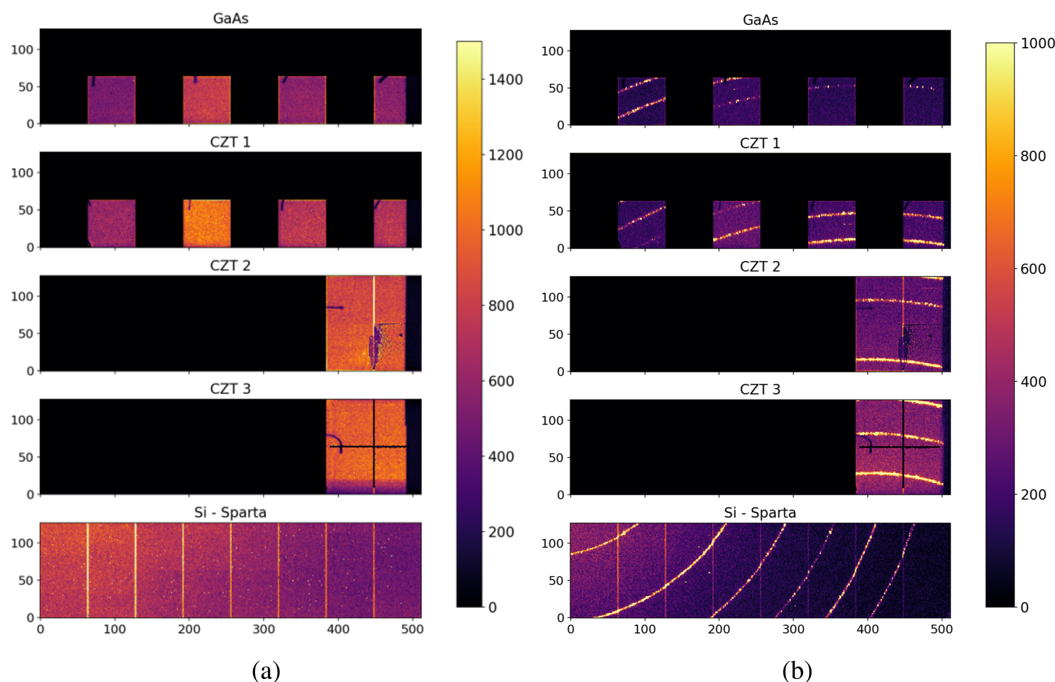

Figure 3. (a) flat-field with YAG fluorescence (run 131/900748), and (b) LaB_6 powder diffraction image taken with the high-Z prototype, with the beam energy set at 24 keV (run 195/900748). The partially covered area for baseline monitoring can be seen on the right side of both images.

2026 JINST 21 C01019

3.1 Intensity scans

At the first beamtime, with the YAG fluorescence setup, the maximum measured flux was 1590 × 14.98 keV photons/mm^2/pulse. The sensors presented good linearity ($R^2 > 0.99$) within this flux range, apart from two single ASICs assembled in positions previously associated with signal integrity issues by the EuXFEL detector group (second-connected ASIC from left to right in the top two FEMs).

At the second beamtime, using homogeneous scattering from a glassy carbon sample at 8.07 keV, it was possible to reach around 2000 ADUs on fixed Medium Gain (corresponding to 2100 × 8.07 keV photons/pixel/pulse). Although no deviation from the linearity was clearly observed, the full-field illumination setup led to other issues, namely the baseline shift associated with bias voltage steps provoked by the charge excess in the sensor, and no conclusive data regarding linearity could be retrieved from the data analysis. This measurement will be replicated in the upcoming campaigns, employing a mask to limit the illuminated area.

3.2 Timing scans

The detection with AGIPD is synchronous to the EuXFEL beam; therefore, a timing scan is a standard procedure to optimize the start time of the acquisition window with respect to the X-ray pulses. Apart from this, useful information can be extracted from comparing the time response of each sensor material, given that their ASICs are synchronized and share the same settings. Figure 4 illustrates the concept: the acquisition window gap is kept constant and the start of the acquisition is scanned in time with respect to the arrival of the EuXFEL pulse.

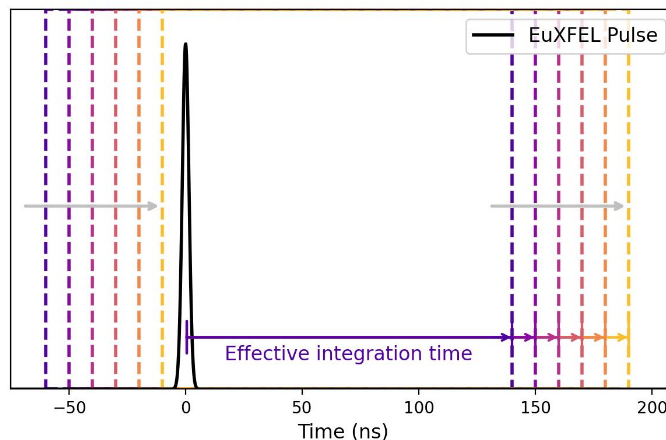

Figure 4. Illustration of a timing scan: the start of the integration window is scanned in time from left to right with respect to the EuXFEL pulse, keeping a fixed width of 200 ns. The effective integration time is scanned from 140 to 190 ns in the picture, starting from the pulse arrival at t = 0.

The start of the acquisition window is scanned by varying an acquisition delay setting that is common for the five FEMs. The delay setting was scanned with 5 ns steps and the acquisitions were taken with an integration time of 200 ns per step. Effectively, the charge integration time after the pulse increases along the scan, until the pulse leaves the acquisition window completely.

2026 JINST 21 C01019

Figure 5 shows the normalized measured intensity, averaged for 50 trains at each step, as a function of the effective integration time for each FEM, for (a) 14.98 keV photons from YAG fluorescence and (b) 8.07 keV photons from glassy carbon scattering. The 0 ns reference in the plot illustrates the inferred time of pulse arrival, 200 ns before the detector starts losing charge. The timing scans were performed in Adaptive Gain mode, using attenuators to ensure low intensities.

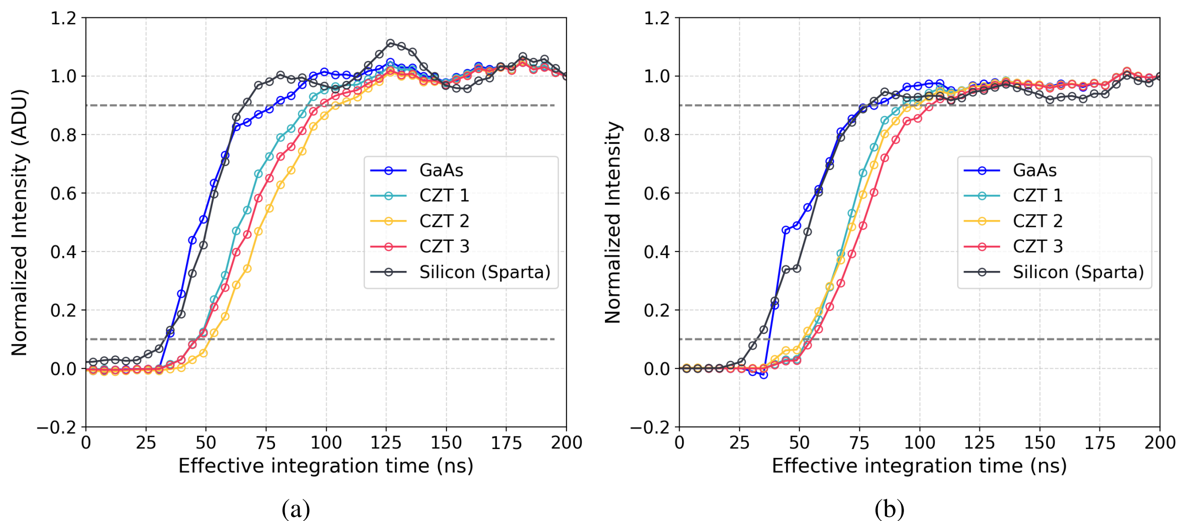

Figure 5. Result from a timing scan at (a) 14.98 keV (run 39/900478) and (b) 8.07 keV (run 30/900516) after smoothing, where a delay between the CZT sensors and Si can be observed. The dashed lines represent the 10–90% thresholds used for the rise time calculation.

It can be seen that the different FEMs do not respond to the beam at the same time. The GaAs sensors had a similar time response to Si, which can be attributed to their similar sensor thickness. The CZT sensors, on the other hand, presented a delay of on average 14 ns with respect to Si for the 14.98 keV experiment, when comparing the curves at 10% of the normalized intensity. This delay could be associated with the small-pixel effect, as the charges are generated very superficially (see appendix A) and have to drift through the sensor thickness before significant current is induced in the electrodes.

Apart from this shift, the high-Z sensors presented a rise time of around 50 ns from 10% to 90% of the normalized intensity at 15 keV, while the Si sensor had a rise time of around 30 ns. The rise times were calculated from a 20-step interpolation between the data points. Detailed results of this analysis are presented in table 2. The measured rise times inherently include contributions from the convolution with the ASIC response and thus cannot be regarded as a direct quantitative measure of charge-transport dynamics within the sensors. Rather, it is the comparative analysis of the temporal responses across different materials that provides physically meaningful insight.

At 8 keV, the sensors presented more uniform rise times around 40 ns, which can be justified by the shallowness of the interaction also at silicon. However, the CZT sensors presented a larger average delay of 21 ns to silicon at 10% of the normalized intensity. The expectation would be to have a similar or smaller delay for lower energies: since the interaction with Si is more superficial (appendix A) for this photon energy, charges would require an additional time, albeit shorter, to drift through the bulk in Si as well. This result could be related to non-uniformities on the electric field close to the cathodes on the CZT sensors, and will be further explored by simulations and future measurements.

2026 JINST 21 C01019

The falling edge of the curves could not be investigated; those results are affected by ASIC effects, traceable to the injection of charges during the reset phase of the pixel electronics.

Table 2. Timing scan results obtained for each sensor material at 14.98 and 8.07 keV.

FEM	14.98 keV (Yttrium fluorescence)		8.07 keV	
	Rise time	Delay to Si at 10%	Rise time	Delay to Si at 10%
GaAs	47.2 ns	1.4 ns	35.3 ns	5.5 ns
CZT1	48.2 ns	12.2 ns	36.7 ns	21.5 ns
CZT2	54.7 ns	18.5 ns	41.7 ns	19.2 ns
CZT3	53.2 ns	12.7 ns	47.2 ns	22.9 ns
Si	29.3 ns	—	41.7 ns	—

3.3 After-signal measurements

The after-signal measurements were taken with LaB_6 powder diffraction in fixed and Adaptive Gain modes, and for different acquisition rates (2.2 and 4.5 MHz, equivalent to integration times of 200 and 120 ns respectively). The effect of the pulse frequency was also explored: the FEL was configured to provide either one pulse per train (effective pulse rate of 10 Hz) or 10 pulses per train with an interval of 1.76 μs between them, for a peak pulse rate of around 0.56 MHz. The data were evaluated by selecting pixels with measured intensity greater than 1000 ADUs (corresponding to 10×24 keV photons in CZT) in the illuminated frame, corresponding to the pixels irradiated by the diffraction rings. The signal in this ROI was then tracked over time along the following frames, focusing on the dark frames between the pulses. The pixels were reset between each individual frame.

In most datasets, only GaAs exhibited some signal after the X-ray pulse. An example of such behavior is depicted in figure 6(a), obtained from a setup of 1 pulse per train, fixed High Gain mode, and detector acquisition rate at 2.2 MHz. The average energy per pixel in the high-intensity ROI, as a percentage of the energy deposited by a 24 keV single photon, is plotted as a function of elapsed time. Figure 6(b) displays images taken with GaAs during the pulse (time = 0) and 909 ns after the pulse.

The attenuation length of 24 keV photons in GaAs is 72.6 μm (appendix A); considering a hole mobility of 200 $cm^2/V{\cdot}s$ [13] and the applied bias voltage of -300 V, the drift time of the holes to the cathode can be calculated to 6 ns. However, the reported lifetime of the holes in this material is 2.5 ns [13]. This means that the majority of the holes are likely trapped or recombined, and their slow release after the pulse could induce a negative current in the anode, explaining the after-signal observed with this detector.

By fitting the exponential decay of the intensity with a double exponential function, two time components are obtained: 1.7 ± 0.3 and 0.20 ± 0.04 μs. The time components are within the expected range of de-trapping times for GaAs [14]. Figure 6 shows an after-signal of less than 12% of one 24 keV photon after 440 ns. In 4.5 MHz acquisition rate data, the observed after-signal corresponded to less than 22% of a 24 keV photon after 220 ns.

2026 JINST 21 C01019

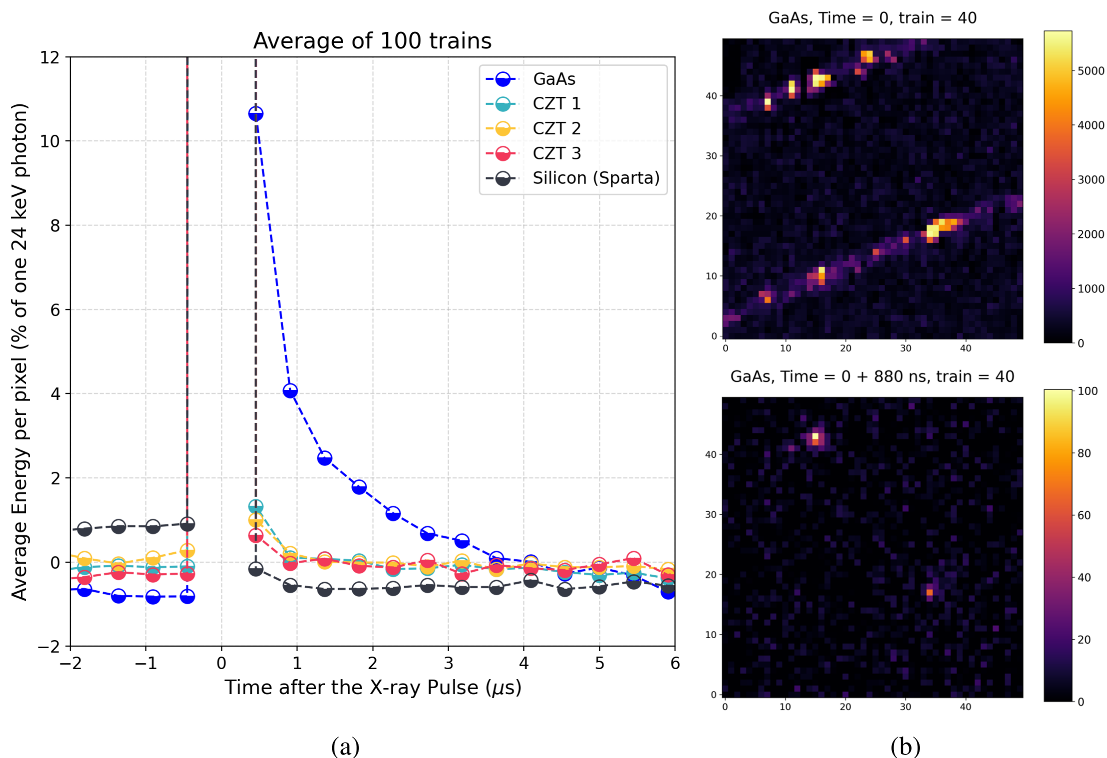

Figure 6. Typical result obtained from the after-signal measurements (run 204/900478): the CZT sensors show little to no signal in the image taken 440 ns after the pulse, while a decaying after-signal lasting up to 3 μs can be observed for GaAs. Figure (a) depicts the signal on the intensity ROI in one sensor of each FEM as a function of the elapsed time, for a dataset acquiring at 2.2 MHz; figure (b) displays the image taken with a GaAs sensor at time 0 (during the pulse) and after 880 ns. It's possible to identify the residual signal in a few heavily irradiated pixels.

In a dataset taken with the ASICs configured to Adaptive Gain mode, a localized high intensity spot was observed in CZT-3. Figure 7 shows a plot revealing an after-signal of energy comparable with GaAs for this sensor (around 8% of a 24 keV photon), which accumulates along the 10 incoming pulses and lasts up to 5 μs after the last pulse in the train. The inset plot shows an image taken during the last pulse of one train, which highlights the intense spot. By fitting the exponential decay of the intensity with a double exponential function, two time components can be extracted: 0.21 ± 0.03 and 2.8 ± 0.2 μs.

It is possible that this spot is related to a Bragg reflection of the beam by a large grain of LaB_6 in the sample, reached after a slight movement of the incoming beam. By the intensity of this spot in Adaptive Gain mode, it is safe to assume that such pixels were in the saturation regime of the Low Gain region during the pulses; from that assumption, the incoming flux can be estimated to be higher than 5000×24 keV photons/pixel/pulse. The after-signal, in contrast, has low intensity and is expected to be back to the High Gain range. By comparing these intensities, one can estimate that the observed after-signal corresponds to less than 0.002% of the incoming pulse intensity. This result is comparable to previously reported after-signal magnitudes for this material [15].

The attenuation length of 24 keV photons in CZT is 118.7 μm (appendix A); according to the weighting potential model for pixelated sensors [16], the drift of the holes in such a superficial layer

2026 JINST 21 C01019

of the sensor should not play a major role in charge induction at the anodes. This hints that other phenomena, e.g. a disruption of the electric field slowing down the electrons, electron traps or even an ASIC effect could be taking place due to the intensity excess. During the second beamtime, when a flux of 2100×8.07 keV photons/pixel/pulse was reached, such an after-signal behavior was not clearly observed in the CZT FEMs.

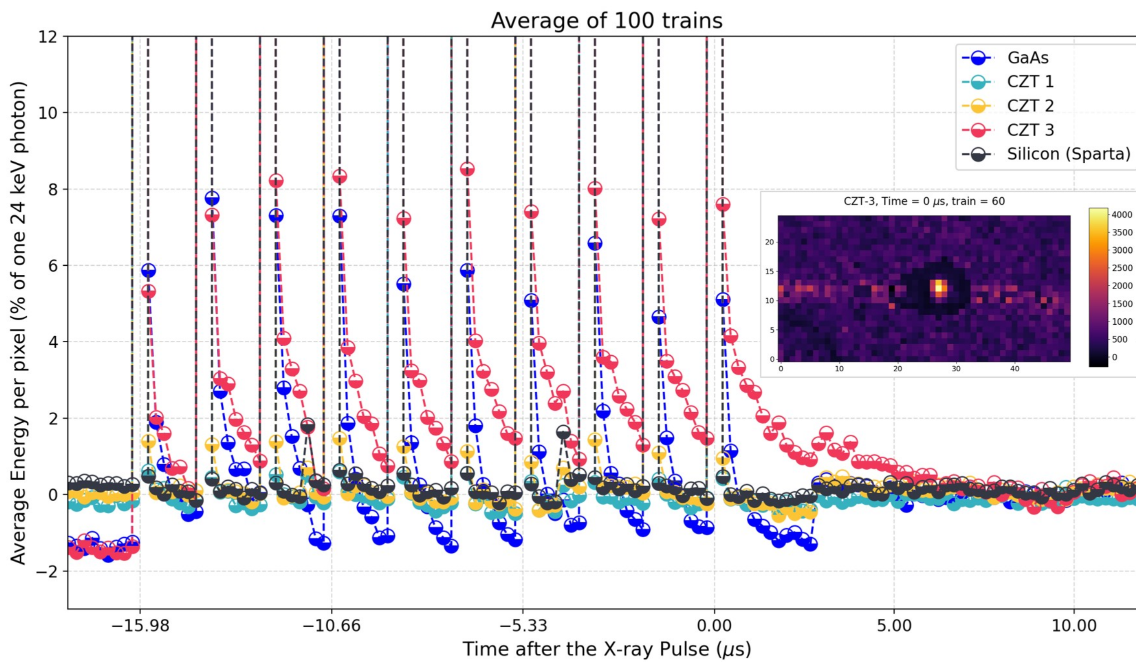

Figure 7. Result obtained during a single-occurrence Bragg diffraction peak at CZT-3 (run 207/900478), showing after-signal comparable to GaAs, which piles-up between the X-ray pulses and lasts up to 5 μs after the last pulse. Inset plot: image of the Bragg diffraction spot during the last pulse of one train.

4 Conclusion and further steps

The CZT sensors hybridized with ecAGIPD ASICs demonstrated encouraging performance for future applications in the HED instrument. Their robustness at high frame rates, elevated photon energies, and high fluxes identifies CZT as the most promising candidate for EuXFEL high-Z sensor detectors. However, aspects of charge transport observed in this study require further investigation, such as charge collection at 4.5 MHz and behavior at photon intensities up to the ASIC limit of $1e{+}04 \times 12$ keV photons/pixel/pulse.

Some improvements are foreseen for the upcoming experiments. A dedicated mask will be manufactured to restrict the irradiated area and mitigate pedestal shifts. In parallel, new efforts are underway to produce n-on-p type silicon sensors compatible with ecAGIPD, a key step toward disentangling ASIC-related effects from intrinsic sensor behavior.

Future work will also expand the characterization of these sensors using synchrotron radiation, laser-based measurements, and dedicated simulations.

2026 JINST 21 C01019

A Sensor material properties considered in this work

Table 3. FEM sensor materials, their respective carrier mobilities ([10, 13]), densities [17] and attenuation lengths [6] at photon energies of 14.98, 24 and 8.07 keV, for reference.

Sensor material	Mobility (e-) (cm^2/V·s)	Mobility (h+) (cm^2/V·s)	Density (g/cm^3)	Attenuation length (µm) 14.98 keV	24 keV	8.07 keV
GaAs	4000	200	5.32	19.9	72.6	28.4
CZT	940	114	5.78	32.2	118.7	8.4
Si	1400	450	2.33	440.4	1770.3	71.5

Acknowledgments

We acknowledge the European XFEL in Schenefeld, Germany, for provision of X-ray free electron laser beam time at the Scientific Instrument HED (High Energy Density Science) (proposals 900478 and 900516) and would like to thank the staff for their assistance.

The authors are indebted to the HIBEF user consortium for the provision of instrumentation and staff that enabled this experiment.

References

[1] A. Allahgholi et al., *The Adaptive Gain Integrating Pixel Detector at the European XFEL*, *J. Synchrotron Radiat.* **26** (2019) 74.

[2] A.P. Mancuso et al., *The Single Particles, Clusters and Biomolecules and Serial Femtosecond Crystallography instrument of the European XFEL: initial installation*, *J. Synchrotron Radiat.* **26** (2019) 660.

[3] A. Madsen et al., *Materials Imaging and Dynamics (MID) instrument at the European X-ray Free-Electron Laser Facility*, *J. Synchrotron Radiat.* **28** (2021) 637.

[4] U. Zastrau et al., *The High Energy Density Scientific Instrument at the European XFEL*, *J. Synchrotron Radiat.* **28** (2021) 1393.

[5] M.C. Veale et al., *Cadmium zinc telluride pixel detectors for high-intensity x-ray imaging at free electron lasers*, *J. Phys. D* **52** (2018) 085106.

[6] J. Hubbell and S. Seltzer, *Tables of X-Ray Mass Attenuation Coefficients and Mass Energy-Absorption Coefficients (version 1.4)*, National Institute of Standards and Technology, Gaithersburg, MD, U.S.A. (1995) [DOI:10.18434/T4D01F].

[7] D. Pennicard et al., *A germanium hybrid pixel detector with 55mum pixel size and 65,000 channels*, 2014 *JINST* **9** P12003.

[8] M.C. Veale et al., *Investigating the suitability of GaAs:Cr material for high flux X-ray imaging*, 2014 *JINST* **9** C12047.

[9] C. Ponchut et al., *Characterisation of GaAs:Cr pixel sensors coupled to Timepix chips in view of synchrotron applications*, 2017 *JINST* **12** C12023.

[10] B. Thomas et al., *Characterisation of Redlen high-flux CdZnTe*, 2017 *JINST* **12** C12045.

2026 JINST 21 C01019

[11] O. Baussens et al., *Characterization of High-Flux CdZnTe with optimized electrodes for 4th generation synchrotrons*, 2022 *JINST* **17** C11008.

[12] H.P. Liermann et al., *Novel experimental setup for megahertz X-ray diffraction in a diamond anvil cell at the High Energy Density (HED) instrument of the European X-ray Free-Electron Laser (EuXFEL)*, *J. Synchrotron Radiat.* **28** (2021) 688.

[13] D. Greiffenberg et al., *Characterization of Chromium Compensated GaAs Sensors with the Charge-Integrating JUNGFRAU Readout Chip by Means of a Highly Collimated Pencil Beam*, *Sensors* **21** (2021) 1550.

[14] A. Dargys, J. Kundrotas, A. Čésna and N. Žurauskiene, *Electric-field-induced ionization of acceptors in p-GaAs*, *Nucl. Instrum. Meth. A* **434** (1999) 71.

[15] B.D. Cline et al., *Characterisation of Redlen HF-CdZnTe at* $> 10^6$ *ph* s^{-1} mm^{-2} *using* $HEXITEC_{MHz}$, 2024 *JINST* **19** P04028.

[16] H.H. Barrett, J.D. Eskin and H.B. Barber, *Charge Transport in Arrays of Semiconductor Gamma-Ray Detectors*, *Phys. Rev. Lett.* **75** (1995) 156.

[17] S. Del Sordo et al., *Progress in the Development of CdTe and CdZnTe Semiconductor Radiation Detectors for Astrophysical and Medical Applications*, *Sensors* **9** (2009) 3491.

2026 JINST 21 C01019